CSIRO PUBLISHING
www.publish.csiro.au/journals/ijwf International Journal of Wildland Fire, 2005, 14, 85–98

Planned Burn-Piedmont. A local operational numerical meteorological model for tracking smoke on the ground at night: model development and sensitivity tests

Gary L. Achtemeier

USDA Forest Service, Southern Research Station, Forest Sciences Laboratory, Athens, GA 30602, USA.
Telephone: +1 706 559 4239; fax: +1 706 559 4317; email: gachtemeier@fs.fed.us

Abstract. Smoke from both prescribed fires and wildfires can, under certain meteorological conditions, become entrapped within shallow layers of air near the ground at night and get carried to unexpected destinations as a combination of weather systems push air through interlocking ridge–valley terrain typical of the Piedmont of the Southern United States. Entrapped smoke confined within valleys is often slow to disperse. When moist conditions are present, hygroscopic particles within smoke may initiate or augment fog formation. With or without fog, smoke transported across roadways can create visibility hazards. Planned Burn (PB)-Piedmont is a fine scale, time-dependent, smoke tracking model designed to run on a PC computer as an easy-to-use aid for land managers. PB-Piedmont gives high-resolution in space and time predictions of smoke movement within shallow layers at the ground over terrain typical of that of the Piedmont. PB-Piedmont applies only for weather conditions when smoke entrapment is most likely to occur—at night during clear skies and light winds. This paper presents the model description and gives examples of model performance in comparison with observations of entrapped smoke collected during two nights of a field project. The results show that PB-Piedmont is capable of describing the movement of whole smoke plumes within the constraints for which the model was designed.

Additional keywords: drainage winds; nocturnal smoke; smoke entrapment; visibility.

Introduction

Slope winds are increasingly recognized as important in the local transport of air pollution and airborne biota. One class of slope wind, the drainage wind, occurs frequently at night when synoptic scale weather associated with high and low pressure systems that produce large-scale wind are relatively weak. At some time during the day (usually near sunset), long-wave radiation from sloping land surfaces exceeds incoming short-wave solar radiation. The land surface and a shallow layer of air just above the surface cool. Minuscule pressure forces combined with negative buoyancy drive cooled air downslope toward valleys. The cool air accumulates in the valleys and either ponds or flows down-valley depending on the slope of the valley floor.

Much research on drainage winds has been conducted in mountainous areas of the world—Australia, Europe, United States (USA), Canada and Mexico. For a list of international local wind studies, see Papadopoulos and Helmis (1999). Wind speeds usually range between 2 and 6 $m\,s^{-1}$ (Post and Neff 1986; Clements *et al.* 1989; King 1989; Neff and King 1989; Sakiyama 1990). Drainage layer depths grow from the valley floor to 200–400 m, usually the depth of steep-sided valleys (Neff and King 1989; Sakiyama 1990). Top-to-bottom temperature differences within these drainage flows are usually 4–5 K (Post and Neff 1986; Neff and King 1989; Sakiyama 1990) giving inversion strengths of 0.01–0.02 $K\,m^{-1}$, although stronger inversions have been recorded (McKee and O'Neal 1989).

Drainage flows also occur in the shallower stream valleys of the Piedmont (Garrett and Smith 1984). Winstead and Young (2000) observed 48 drainage flows exiting from valleys in Maryland onto Chesapeake Bay. Piedmont drainage flows are typically shallow and weak. They form predominately when larger scale circulations are weak (light winds) and when radiational cooling maximizes pressure forces and negative buoyancies within drainage airmasses (clear skies). These concurrent events occur within anticyclones (Lavdas and Achtemeier 1995).

The Piedmont is a low plateau roughly 100–300 km wide and 1500 km long extending down the south-east USA from Maryland to Alabama. It separates the Atlantic Coastal Plain and Gulf Coastal Plain from the Appalachian Mountains. The Piedmont rises from ~200 m along the coast-facing side to ~400 m on the mountain-facing side. The Piedmont is highly

 10.1071/WF04041 1049-8001/05/010085

eroded into a network of interlocking ridges and valleys. Ridge/valley elevation differences typically range from 20 to 50 m.

Piedmont drainage flows are subject to disruption by larger-scale wind systems (Achtemeier 1993). Synoptic scale pressure fields can exceed weak pressure fields within drainage flows. When this happens, drainage flows can be reversed to blow up-drainage and smoke and other pollutants transported into side valleys and/or into adjacent valleys through gaps in ridges. Transport of smoke into adjacent valleys presents a challenge for numerical modeling if the goal is an operational model. It is no longer practicable to define a model grid to enclose a single valley or even the valley and its tributaries (O'Steen 2000), or to compress a grid domain for the valley of choice (Varvayanni *et al.* 1997). The model domain must be extended several tens of kilometers to enclose adjacent drainage systems with the same resolution as that for the target valley.

Knowledge of air movement near the ground at night is important to land managers who use prescribed fire in the management of forest and agricultural lands. A prescribed fire is planned and set subject to fire safety and air quality regulations to accomplish a predefined management objective. Although the vast majority of prescribed burns are completed without incident, there are occasions when smoke from smoldering fuels persists after sunset and becomes entrapped within slow-moving drainage flows. Entrapped smoke can drift into populated areas and impact residents, particularly those with respiratory problems. Smoke-laden air masses can drift across roadways and contribute to poor visibility. Smoke and associated fog have been implicated in multiple-car pile-ups that have caused numerous physical injuries, heavy property damage and fatalities (Mobley 1989).

Planned Burn (PB)-Piedmont is an operational numerical weather and smoke model designed to simulate near-ground smoke transport at night. The sections to follow present brief descriptions of the constraints placed on an operational numerical drainage flow/smoke model, model assumptions, model equations, a method to solve the model equations, and examples of smoke transport simulations over the complex interlocking terrain of the Piedmont of the South.

PB-Piedmont: assumptions and model theory

PB-Piedmont is designed to predict the transport of smoke trapped near the ground at night over complex interlocking ridge/valley systems typical of the Piedmont. The operational requirements are that PB-Piedmont must be installed on desktop computers operated by land managers. The model must be capable of being run by those with little computer experience and no experience in meteorological modeling. The model must generate timely predictions if it is to be a factor in decision-making.

PB-Piedmont must be able to model smoke on the terrain scales through which local circulations transport smoke. The grid scale must be fine enough to resolve shallow gaps in ridges. The grid must be large enough to enclose adjacent drainages when necessary. Therefore, to satisfy the spatial requirements and to produce timely predictions, the number of calculations must be minimized. It is required that the mathematics be simple and the physical terms describing complex processes be simplified or replaced with empirical terms.

Basic model assumptions

The model design depends on several assumptions regarding the meteorology of the Piedmont. First, Achtemeier (1993) found that Piedmont drainage flows were typically 15 m deep and generated down-valley winds as slow as 0.2 m s^{-1}. Shallow drainage layers can be 'vertically integrated', meaning that air movements within the layer are approximated by the mean wind for the layer. The vertically integrated approach has been used successfully by Garrett and Smith (1984) and O'Steen (2000). Entrapped smoke is a passive tracer and is assumed to be uniformly distributed through the depth of the drainage layer. The model therefore is not appropriate for simulating nocturnal smoke movement in the mountains because drainage flows there may be much deeper and internal circulations may become significant in transporting smoke.

Second, it is assumed that the meteorology of the Piedmont during clear sky and light wind episodes (prevailing weather when most smoke entrapment occurs) consists of two scales of motion—the synoptic scale pattern of low- and high-pressure centers and fronts, which can be described by the National Weather Service network of surface weather stations, and the drainage scale (meso-beta), which is characterized by the terrain of the Piedmont. Weather disturbances that are too small to be resolved by the existing network of surface stations (meso-alpha) are assumed to be negligible or non-existent. The model therefore is not appropriate for simulating nocturnal smoke movement near the coasts or large lakes where there are land breezes.

Third, because the domain size is limited, it is assumed that regional scale temperatures, winds and pressure data needed by the model can be represented by single values interpolated from surrounding weather stations to the location of the prescribed burn.

Fourth, it is assumed that the drainage layer airmass is effectively 'decoupled' from overlying airmasses. Near sunset, under conditions of light winds and clear skies, the ground and the air immediately above it cool rapidly. Mixing with the overlying airmasses ceases as the stable drainage airmass deepens. Decoupling makes it possible to model just the meteorology of the drainage layer.

Governing equations

Figure 1 shows the schematic structure of the PB-Piedmont model. The drainage layer is defined as a sublayer within

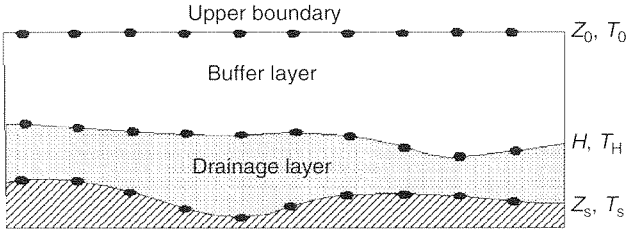

Fig. 1. Vertical structure of the PB-Piedmont numerical wind model. Dots represent grid points.

the nocturnal boundary layer that initially overlays the whole domain—ridge tops and valley bottoms. This is done to satisfy constraints of spatial continuity throughout the model domain. The drainage layer extends from the surface, Z_S, to a height, H, defined as the top of the drainage layer. Above it a buffer layer (also within the nocturnal boundary layer) extends from H to Z_0, a level of constant height 100 m above the highest ground as defined from the elevation data within the model domain. It is assumed that Z_0 is a level of constant pressure. This assumption is not severe when PB-Piedmont is run under weak anticyclonic conditions. The assumption of a vertically integrated drainage layer constrains the definition of the vertical coordinate for PB-Piedmont as one bounded by H–Z_S. The lower coordinate surface follows the terrain, Z_S. The upper coordinate follows the top of the drainage layer, H. The vertical coordinate is defined by,

$$S = (H - z)/(H - Z_S). \tag{1}$$

The Lagrangian difference forms for the drainage layer prognostic equation for the layer mean wind components, u and v, per unit mass, are,

$$\begin{aligned}\frac{\Delta u}{\Delta t} &= -\left\{R\overline{T}\frac{\Delta \ln(p)}{\Delta x} + g\left[(1-S)\frac{\Delta H}{\Delta x} + S\frac{\Delta Z_S}{\Delta x}\right]\right\} \\ &\quad + fv + m_x(U-u) - \frac{1}{(H-Z_S)}C_D u\sqrt{u^2+v^2} \\ \frac{\Delta v}{\Delta t} &= -\left\{R\overline{T}\frac{\Delta \ln(p)}{\Delta y} + g\left[(1-S)\frac{\Delta H}{\Delta y} + S\frac{\Delta Z_S}{\Delta y}\right]\right\} \\ &\quad - fu + m_y(V-v) - \frac{1}{(H-Z_S)}C_D v\sqrt{u^2+v^2},\end{aligned} \tag{2}$$

where R is the gas constant for dry air, $\overline{T}$ is the mean temperature over the difference interval, and g is the acceleration of gravity. See Table 1 for a list of definitions of the variables that appear in the mathematical equations.

The forcing functions are described as follows:

(1) The pressure gradient terms of the hydrodynamic equations transformed into the 'S'-coordinate system are enclosed in braces. Over sloping surfaces, the pressure gradient in the sigma coordinate system is expressed by two terms, in this formulation, the $\ln(p)$ term and the bracketed term multiplied by gravity. These terms can be large and are of opposite sign. Thus, the pressure gradient over sloping surfaces can be the small difference between large values. Achtemeier (1991) showed that the taking of differences of pressure over sloping coordinate surfaces can generate hydrostatic truncation errors of magnitude sufficient to overwhelm the minuscule pressure forces that drive Piedmont drainage flows. The problem can be eliminated if the pressure at any grid point is calculated downward from the top of the model domain by stepping down in thin layers of thickness no greater than 10 m.

Table 1. Definitions of the variables that appear in the mathematical derivations

Variable	Definition
C_D	Drag coefficient
c_r	Coefficient of scatter for the smoke particle generator
C_T	Drainage layer cooling rate (2.78×10^{-3} K s^{-1})
D_r	Drainage layer replenishment rate (5×10^{-4} m s^{-1})
f	Coriolis parameter
g	Acceleration of gravity (9.8 m s^{-2})
h	Depth of the drainage layer (m)
H	Height of the top of the drainage layer (m)
k	Shape factor for the Gaussian weight function (m^2)
m_x, m_y	x, y components of the mixing coefficient (5×10^{-4})
p	Pressure
R	Universal gas constant (287.04 m^2 s^{-2} K^{-1})
R_e	Frequency response for the A-Function
s	Coordinate oriented along valley-axis
S	Hybrid terrain—and drainage layer height—following vertical coordinate system
t	Time (s)
T	Temperature (K)
T_H	Temperature (K) at the top of the drainage layer
T_0	Temperature (K) at the top of the model domain
T_R	Reference synoptic temperature (K) taken 3 h before sunset and interpolated to the fire location from National Weather Service hourly weather data
T_S	Synoptic scale temperature (K) interpolated to the fire location from National Weather Service hourly weather data
$\overline{T}$	Average temperature as specified
u, v	x, y-component of the model drainage layer horizontal mean wind (m s^{-1})
U, V	x, y-component of the observed surface wind interpolated to the burn site from surrounding weather stations
U_{max}	Maximum wind speed found in the model domain at a given time
u_g	Geostrophic wind
x	x (east direction)
y	y (north direction)
z	Up as defined in the modified sigma coordinate
Z_S	Ground surface elevation (m)
Z_0	Height (m) at the top of the model domain
δ_1, δ_2	Weights for the cooling function
γ	Drainage layer lapse rate of temperature (K m^{-1})
Γ_d	Dry adiabatic lapse rate of temperature (0.01 K m^{-1})
λ	Wavelength (m)

(2) The Coriolis terms (second terms of equation 2) represent the impact of the earth's rotation on the existing wind. The Coriolis force turns the wind to the right of its existing motion in the northern hemisphere. The parameter f is a function of the latitude and the rotation rate of the earth. The terms are small but they can impact the movement of slow drainage flows over flat basins.

(3) The third terms couple/decouple the modeled drainage layer with the synoptic scale wind (U, V) supplied as an upper boundary condition. For the heated part of the day the bulk mixing coefficients (m_x, m_y) are set to $5 \times 10^{-4}\ \mathrm{s}^{-1}$ to drive the solution to the synoptic scale wind. Then, using the synoptic scale temperature for 3 h before sunset as a reference temperature, T_R, the coefficients are allowed to decrease to 0.0 when the temperature has cooled 2 K from T_R. This step simulates the nocturnal transition period just before sunset (Achtemeier 1993). The exact functional form for the coefficients is not critical to PB-Piedmont as the important drainage layer forcing begins after sunset.

(4) The friction terms (last terms of equation 2) are weighted inversely by the depth of the drainage layer. The deeper the drainage layer, the less is the frictional drag on the vertically integrated airmass. The bulk drag coefficient for a southern pine forest is $C_D = 10^{-2}$ (Garrett and Smith 1984). The Piedmont land cover is typically southern pine forest interspersed with open fields—clearings for dwellings, pasture lands, thinned plots or cut-over areas. Thus part of the Piedmont land cover could be represented as grassland with $C_D = 10^{-3}$. Sensitivity tests revealed that drainage winds generated by the terrain of the Piedmont overwhelm forcing generated by differences in land use. Land use forcing is constrained to modulating the rate of down-valley flow and causing minor within-valley wind deflection and channeling. Thus, it is not unreasonable to set $C_D = 10^{-2}$ for the whole domain.

The Lagrangian difference forms for the drainage layer prognostic equations for height and temperature are:

$$\begin{aligned} \frac{\Delta H}{\Delta t} &= \frac{\Delta Z_s}{\Delta t} + (H - Z_s)\left(\frac{\Delta u}{\Delta x} + \frac{\Delta v}{\Delta y}\right) + D_r \\ \frac{\Delta T}{\Delta t} &= \frac{\Delta H}{\Delta t}\Gamma_d + \frac{\Delta T_s}{\Delta t_h} + \delta_1 \delta_2 C_T. \end{aligned} \tag{3}$$

Drainage layer height is adjusted for air movement over unlevel terrain (first term) and deepening within a divergent wind field (second term). The third term (D_r) represents the drainage layer replenishment rate during the course of the night. The drainage layer (not to be confused with the nocturnal boundary layer: Achtemeier 1993) is assumed not to exceed two-thirds the depth of Piedmont valleys (approximately 50 m). Thus the drainage layer is allowed to grow 24 m over a typical 12 h nocturnal period in addition to the initial 10 m depth of the layer. Therefore, cooled air that drains from the ridges into the valleys is constantly replenished at a rate of $2\ \mathrm{m\,h^{-1}}$ ($5 \times 10^{-4}\ \mathrm{m\,s^{-1}}$). Furthermore, in the absence of confirming data, the drainage layer replenishment rate is assumed to be constant in time and uniform in space.

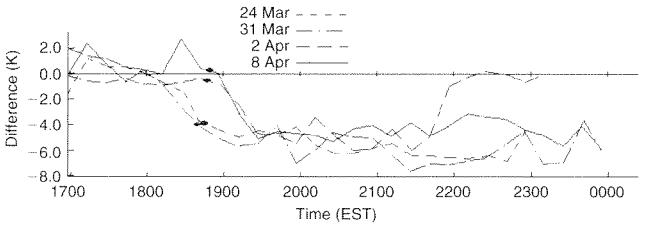

Fig. 2. Time series of the difference in temperature between a ridge and a basin site for the following dates in 1992: 24 March, 31 March, 2 April and 8 April. The elevation difference is 30 m.

Temperature is adjusted as follows. The first term is an adiabatic adjustment for changes in the height of the drainage layer. These include adjustments for movement over changing elevation, deepening caused by a convergent wind field, and drainage layer replenishment. The second term represents synoptic scale cooling (heating) defined as the difference between two consecutive hourly observations of temperature (T_s) interpolated to the center of the model grid from surrounding National Weather Service surface weather stations and thence converted into cooling (heating) rate in K/s by dividing by 1 h (Δt_h).

The third term represents cooling within the drainage layer after sunset. The local cooling rate is generated within PB-Piedmont and applies to the temperature at the ground. It was derived from observations of cooling within a basin during clear skies at night (Achtemeier 1993) and confirmed by other observations of local inversion formation in the Piedmont areas of the South. Figure 2 shows a time series of the temperature difference between a valley site and a ridge-top site (elevation difference of 30 m) on four nights during March–April 1992. Negative differences occur when the basin is colder than the ridge. Figure 2 shows that, on all four nights, temperature differences were approximately zero before sunset (identified by the shaded circles between 1845 and 1900 EST). Differences dropped to approximately −5 K within 0.5 h of sunset as the valley cooled much more rapidly than did the ridge. Thereafter cooling in the valley was approximately the same as cooling on the ridge. Temperature differences averaged approximately −5 K after 1930 EST. An exception was the night of 2 April when gusty winds after 2145 EST mixed out the valley, a frequent occurrence for shallow drainage flows (Gudiksen *et al.* 1992).

Based on Fig. 2, the maximum within-drainage-layer cooling rate is $C_T = 2.78 \times 10^{-3}\ \mathrm{K\,s^{-1}}$. However, the actual cooling is determined by the coefficients that take on the

following values:

$$\delta_1 = \begin{cases} 0 \text{ if before sunset} \\ 1 \text{ if after sundown} \end{cases}$$

$$\delta_2 = \begin{cases} 0 \text{ if } \gamma \geq \gamma_R \\ 1 \text{ if } \gamma < \gamma_R \end{cases},$$

where

$$\gamma = \frac{(T_H - T)}{H - Z_s}.$$

The first coefficient allows for cooling within the drainage layer only after sunset. The second coefficient is designed to prevent the development of excessive lapse rates of temperature within shallow layers. For each time step, the drainage layer lapse rate of temperature, γ, is calculated as the difference between the temperature at H (T_H) and the surface temperature, divided by the depth of the drainage layer. Based on Fig. 2, under dry conditions, cooling is stopped when γ exceeds a reference lapse rate, $\gamma_R = 0.1667\ \mathrm{K\ m^{-1}}$.

Additional corrections are made for moist conditions. As the air temperature falls to the dew point temperature, dew formation commences beginning first in the cooler basins. Latent heat release slows the rate of cooling but the removal of water dries the air thus lowering the dew point temperature slightly. PB-Piedmont allows the dew point temperature in valleys to fall no more than 1.75 K below the dew point temperature interpolated to the center of the model grid from surrounding National Weather Service surface weather stations.

The use of empirical cooling functions is preferred over complicated time-dependent cooling equations for three reasons. First, simple empirical relations require little computational power and seem justified with respect to other simplifying assumptions in the design of PB-Piedmont such as the vertically integrated drainage layer. Second, land surface conditions such as soil moisture, ground cover and soil type will not be available to most users of PB-Piedmont. Third, average cooling rates should apply to a first approximation for weather conditions of clear skies and light winds for which PB-Piedmont is applicable.

Integration methods for PB-Piedmont

PB-Piedmont uses a downstream-stepping semi-Lagrangian scheme—a departure from most semi-Lagrangian methods, which are upstream-stepping schemes. Staniforth and Cote (1991) provide a general review of upstream-stepping schemes. The downstream-stepping approach is used because terrain is not smoothed in PB-Piedmont. For highly divergent drainage flows over the complex terrain of the Piedmont, it may not be possible to accurately define back-trajectories needed for upstream-stepping methods. The time step, valid for the whole domain, is calculated internally subject to the Courant, Friedrichs, Levy (CFL) linear stability criteria ($U_{max}\Delta t/\Delta x < 1$) (Thompson 1952). The time step is defined by half the grid spacing divided by the maximum velocity found in the domain. Velocity component changes at each grid point are found by multiplying equation (2) by the time step. Then each point is moved forward a distance equal to the product of the total velocity (existing velocity plus velocity change) with the time step through the predictor–corrector method developed for streamlines by Achtemeier (1979) and expanded for trajectories (Scott and Achtemeier 1987). The state variables, T and H, are carried to the new locations along with the velocity. Temperatures are adjusted adiabatically for changes in elevation.

The interpolation step: the A-Function

Upon completion of the Lagrangian downstream step, the new field of points is no longer located at grid square intersections but is quasi-regularly distributed over the grid. The next step is to recalculate the properties of the field at the grid square intersections via interpolation of properties from the surrounding field of points. Various interpolation methods have been used for upstream-stepping semi-Lagrangian methods; the most widely used being cubic spline interpolation (Staniforth and Cote 1991). Ritchie (1986) devised a scheme to eliminate interpolation and the associated smoothing. However, these schemes are specific to the upstream-stepping method.

An objective analysis or surface fitting scheme is appropriate for gridding quasi-regularly distributed data. The behavior of the Gaussian function as a weight function for successive corrections interpolation of meteorological data has been studied by Barnes (1964, 1973, 1994), Achtemeier (1987, 1989, 1994), Pauley and Wu (1990) and others. Barnes (1964) produced a theory of how the Gaussian interpolation scheme smoothes data as a function of wavelength and reinterpolation. Knowledge of the response characteristics for an interpolation scheme is useful when deriving a local mass balance restoration equation.

Successive corrections interpolation requires:

(1) An estimation of the value of a function at points on a grid by interpolation from surrounding data points;
(2) An estimation of the value of the function at the data points by reinterpolation from the surrounding grid points; and
(3) An improvement in the estimation of the function at the grid points by adding an additional interpolation of the discrepancies found in step (2) to the original estimation.

Conceptually, steps (2) and (3) can be repeated indefinitely at great computational cost to cause the estimation to converge toward, but not always to, the original function. The data generated by the Lagrangian step in PB-Piedmont are quasi-regularly distributed, are error-free, and correctly resolve the motion scales carried in the model. Thus interpolation smoothing should be minimized or eliminated, if possible.

Table 2. A-Function theoretical response and measured response for analysis of equally spaced data for wavelengths ranging from $48\Delta x$ to $2\Delta x$, with Δx being the separation between grid points
$4k = 1.40; 0.70$

Wavelength	Theoretical response	Measured response
48	1.0000	1.0002
24	0.9999	1.0006
16	0.9993	1.0009
12	0.9978	1.0006
8	0.9896	0.9964
6	0.9697	0.9829
4	0.8776	0.9154
3	0.6143	0.7424
2	0.3242	0.6474

In the derivation found in Appendix 1, the restorative properties of the Gaussian function are investigated and the results used to derive an algorithm—the A-Function—that reproduces the accuracy of the successive corrections methods but without the need for steps (2) and (3). Achtemeier (1989) found that the Gaussian weight applied to data distributed on a regular mesh restores more of the short wavelengths than predicted by theory. Table 2 compares the theoretical responses calculated from equation (A8) with the measured response (defined as the ratio between the amplitude restored by the A-Function applied to regularly spaced data and the amplitude of the original function) for the range of wavelengths from $48\Delta x$ to $2\Delta x$. Here Δx is the spacing between grid points.

The overall impact of the departure from theory is to increase the robustness of the A-Function. The A-Function amplifies all wavelengths, with the greatest amplification being for the shorter waves. With the choices for $4k$ in Table 2, the measured response is slightly greater than 1.0 for the longer wavelengths, meaning that the A-Function produces a slight amplification of these waves. Thus the wind components, temperatures and depths of drainage flows are not smoothed for valleys for which ridge-to-ridge distances are defined by eight or more grid points. Shorter wave features are smoothed. For example, the A-function smoothes ~9% of drainage flows within ravines defined by the $4\Delta x$ wave, and $2\Delta x$ features are smoothed by 36% per time step.

Drainage layer mass adjustment

For each time step, the field being interpolated is smoothed non-uniformly through application of the A-Function. In PB-Piedmont, interpolation is done on u, v, T and the thickness of the drainage layer, $h = H - Z_S$. Table 2 shows that amplitudes of wavelengths smaller than $8\Delta x$ suffer smoothing. Thus drainage flows within small-scale features such as deep ravines will become weaker, warmer and shallower. Drainage flows within larger valleys and basins will be largely unaffected by the A-Function.

PB-Piedmont replaces some of the mass lost by interpolation through a mass redistribution function. The integrated or total mass loss over the whole model domain can be found by taking the difference between the total mass at successive time steps and correcting for the mass lost or gained through the lateral boundaries of the domain and drainage layer replenishment. The model equations are normalized by unit mass. Therefore the mass change is represented by the change in the volume of the drainage layer domain or, in reference to the S-coordinate system, the volume of the layer contained below H. The volumes of the drainage layer domain at the current time step and at the previous time step, corrected for drainage layer replenishment, D_r, are given by

$$V^t = (\Delta x)^2 \sum_{i=1}^{m} \sum_{j=1}^{n} h_{i,j}$$
$$V^{t-1} = (\Delta x)^2 \sum_{i=1}^{m} \sum_{j=1}^{n} (h_{i,j}^{t-1} + D_r). \tag{4}$$

The volume of the drainage layer passed through the boundaries of the model domain is

$$V_b = \Delta x \Delta t \left[\sum_{i=1}^{m} (h_{i,1} v_{i,1} - h_{i,n} v_{i,n}) + \sum_{j=1}^{n} (h_{1,j} u_{1,j} - h_{m,j} u_{m,j}) \right]. \tag{5}$$

The volume replacement to be added to the total volume so that total volume is conserved is then

$$V_d = (V^{t-1} + V_b) - V^t. \tag{6}$$

However, because the horizontal dimensions of the domain are fixed, the volume replacement is equivalent to adjusting the layer depth for the layer depth discrepancy. The adjusted layer depth is

$$h_{i,j}^{adj} = h_{i,j} + V_d \left(\frac{h_{i,j}}{V^t} \right). \tag{7}$$

Total drainage layer volume (mass) is conserved by equation (7); however, the replacement of mass is not uniform. The greatest mass replacement occurs where the drainage layer is deepest, namely in the valleys. Therefore, for the interpolation/mass correction cycle of a given time step, long wavelength ($>8\Delta x$) valleys, which were unsmoothed by interpolation, receive mass through equation (7) and thus gain mass. Short wavelength valleys receive mass through equation (7) but not at sufficient magnitude to compensate for mass loss through interpolation.

Initial and boundary conditions and synoptic time stepping for PB-Piedmont

In keeping with the assumptions described at the beginning of this section, the vertical structure of the model atmosphere

is in two layers, the shallow drainage layer near the ground and a buffer that extends from it to an elevation of 100 m above the highest terrain. Figure 1 summarizes the layer division along with model details. Initial temperature, dew point temperature and wind components are interpolated from surrounding National Weather Service surface weather stations to the location of the burn site by using a Gaussian scheme developed by Barnes (1964, 1973) and optimized by Achtemeier (1987, 1989) for objective analysis of quasi-regularly spaced data. Horizontal pressure gradients are interpolated with a variant of the direct derivative method developed by Caracena (1987).

These interpolated synoptic scale weather data are used to develop the initial upper boundary as follows. The procedure should be started at least 3 h before sunset to assign the reference temperature for the mixing coefficients in equation (2). The lapse rate of temperature for the buffer layer can vary with time but is constant in space. The initial buffer layer lapse rate is dry adiabatic. The initial drainage layer depth (H) is 10 m and the initial drainage layer lapse rate of temperature is also dry adiabatic. The temperature (T_0) at the top of the model domain (Z_0) is calculated by adjusting the synoptic temperature dry adiabatically for the difference in elevation between the elevation of the burn site and the top of the model domain. Then the temperatures at H and Z_s at each grid point are calculated adiabatically from Z_0 to the top of the drainage layer and the ground.

The wind and pressure fields for the drainage layer are initialized with the synoptic wind components and horizontal pressure gradients.

After the initial conditions are specified, PB-Piedmont is run out to 30 min past the hour. The model pauses for new data to update the synoptic weather for the next hour. Then the model is run from 30 min before the hour to 30 min past the hour. The above procedure is repeated for each hour so that the model runs with centered time differences for synoptic weather.

In its current design, PB-Piedmont is predictive but must wait for the availability of key boundary data. When numerical model prediction data become routinely available for forestry users, PB-Piedmont will be made fully predictive.

Elevation data

Critical for accurate modeling of the smoke movement near the ground at night is specification of the lower boundary. Smoke can be entrapped in small basins, flow along road and stream cuts or through small gaps in ridges. Therefore, the model requires very fine scale spatial resolution and accurate elevation data in order to model smoke on the terrain scales through which local circulations transport smoke. The US Geological Survey's 30 m digital elevation model (DEM) data provide the lower boundary for PB-Piedmont. The horizontal grid spacing is set by the user within the range 30 m (the minimum spacing of USGS DEM elevation data) to 150 m (larger spacing degrades ground features in terrain characteristic of the Piedmont).

Smoke particle generator

Residual smoke is assumed to occur anywhere within an area burned. The area burned, supplied by the user, is converted to a square centered at the coordinates given for the burn. A 5×5 grid is laid over the square and 25 particles per time step are released at the grid intersections. These particles serve as tracers carried by the local winds. The 25-point grid requires that all parts of the burn area contain smoke sources.

Particle locations are moved with the local winds generated within PB-Piedmont. The new locations are found through the predictor/corrector method for generating streamlines (Achtemeier 1979). However, because all particle transport is by mean flow within a vertically integrated domain, the particles will eventually converge to a line at the centers of valleys. To account for re-circulations and small-scale turbulence within the drainage layer wind field, the particle locations are subjected to additional displacements through

$$\begin{aligned} x_{\text{new}} &= x + c_{\text{r}}(0.5 - x_{\text{r}}) \\ y_{\text{new}} &= y + c_{\text{r}}(0.5 - y_{\text{r}}), \end{aligned} \tag{8}$$

where $c_{\text{r}} = 0.25$ and $0 < x_{\text{r}}, y_{\text{r}} < 1$ are random numbers. This choice for coefficients for equation (8) allows maximum horizontal displacements of up to 12% of a grid separation per time step and these are independent of the mean air flow within drainage layers. However, given that the displacements can be of either sign, cumulative displacements are relatively small. For a large number of particles in a uniform wind field, equation (8) yields a Gaussian distribution.

PB-Piedmont does not calculate smoke concentrations. The amount of material engaged in smoldering may vary greatly within a burn area and among burn sites. Thus the smoldering emission rates for a particular burn are poorly known. Therefore the primary contribution of PB-Piedmont to the smoke management problem is in providing an answer to the question: 'Where does the smoke go?'

PB-Piedmont validation through aerial photography and surface temperature observations

Tests with PB-Piedmont show that the combination of synoptic scale wind systems with weak drainage winds that form over terrain typical of the Piedmont of the south-east can distribute smoke in complex plumes and patches. Valley orientation with respect to the winds and with respect to adjacent valleys, steepness of slopes, locations of gaps in ridges, and valley depth can make the difference between entrapment and ventilation. Modeled smoke can be transported among valleys through small gaps in ridges. Whether these complex smoke plume patterns exist is a subject for model validation.

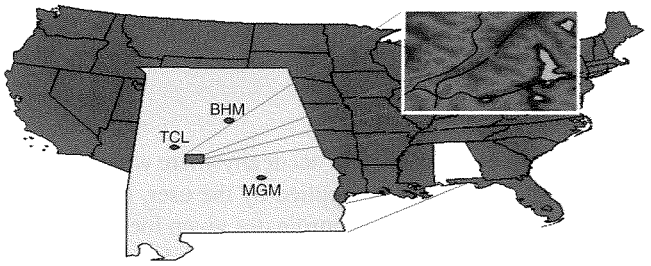

Fig. 3. Location of the site of experimental burns conducted at the Oakmulgee Wildlife Management Area in Alabama during March 1997 in relation to three nearby weather stations.

Existing observations on smoke movement at night are few. Data exist as locations of highway accidents where smoke was implicated as a causal factor and recorded reports of smoke by personnel who drive on highways surrounding burn sites searching for smoke incursions. Data on the movement of entire smoke plumes near the ground at night have been non-existent. Therefore, a key factor in the validation of PB-Piedmont is obtaining observational data on the movement of a whole smoke plume near the ground at night.

A video camera equipped with a light-enhancing device and an infrared cut-off filter was mounted in a Beechcraft King Air aircraft and flown over an experimental burn site at the Oakmulgee Wildlife Management Area located in the Talladega National Forest in western Alabama (Achtemeier *et al.* 1998) (Fig. 3). The site was selected for terrain typical of the Piedmont, safety and the absence of light sources. The site was located along a service road at the bottom of a stream basin that flowed to the north-east. Smoke was observed successfully and recorded during the evenings of 20 and 21 March 1997. Raw video images, methods of image analysis and resulting smoke distribution relative to surrounding landforms were described for 20 March 1997 by Achtemeier (1998) and Achtemeier *et al.* (1998). These results, along with results from 21 March 1997 are compared with simulations from PB-Piedmont in the following paragraphs.

20 March 1997

Modeling smoke movement for the night of 20 March 1997 was a difficult test for PB-Piedmont. Beginning at 2145 local standard time (LST), Forest Service ground personnel ignited 50 bales of hay soaked in diesel fuel along a road next to a stream basin that flowed to the north-east. Once the hay bales were flaming vigorously, the fire was extinguished with water. The bales then smoked profusely. Ground crews also detonated 60 smoke bombs that had burn lifetimes of ~2 min each. Aircraft overflights at ~1500 m altitude commenced at 2148 LST and continued at 7-min intervals for 2 h.

The project forecast called for winds to decrease to near-calm with rapid cooling in the basin to entrap smoke there. Drainage and valley flows favored slow movement of smoke down-valley to the north-east.

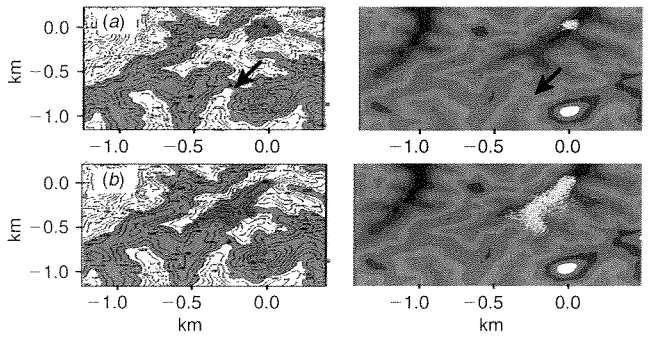

Fig. 4. Left panels: Image analysis of smoke plume on night of 20 March 1997 overlain on 30 m DEM elevation data. Right panels: PB-Piedmont simulation of smoke for the corresponding time—(*a*) 2150 LST and (*b*) 2215 LST. Arrows identify gap in ridge enclosing stream valley.

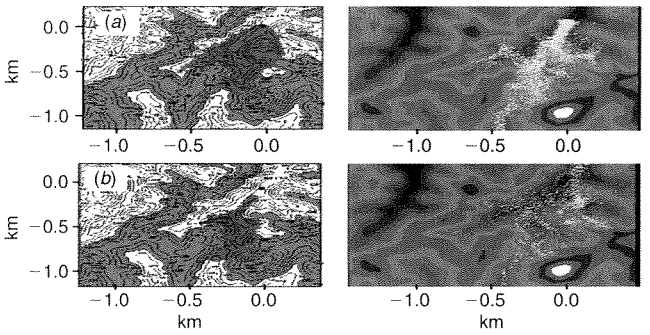

Fig. 5. Same as Fig. 4 except for (*a*) 2255 LST and (*b*) 2354 LST.

Figure 4 compares smoke movement relative to the surrounding elevation as extracted from video imagery with PB-Piedmont simulations for the first half of the experiment. All elevations are measured above mean sea level (msl). Elevations range from 100 m in the bottom lands to around 150 m along the ridge tops with a few high points near 170 m. Elevations greater than 130 m are shaded to better identify the drainage basin. Elevations above 135 m are shaded differently to highlight a 10 m deep gap in the ridge enclosing the southern end of the valley (arrows). Smoke generated at the burn site (Fig. 4*a*) did not move down-valley as expected. Instead, the smoke moved south-westward up-valley along the natural extension of the stream (Fig. 4*b*). Then the plume shifted to impinge directly upon a protruding ridge.

PB-Piedmont was initialized and updated with hourly observations of temperature, humidity, pressure and wind speed and direction as interpolated from the surrounding National Weather Service surface weather observing network. The right panels of Fig. 4 show smoke movement generated by PB-Piedmont for the corresponding times as observed in the left panels. Model smoke moves up-valley and divides around the protruding ridge.

During the last half of the experiment the smoke plume split around the ridge (Fig. 5*a*), flowed up a side valley and crossed the ridge through the shallow gap at the southern

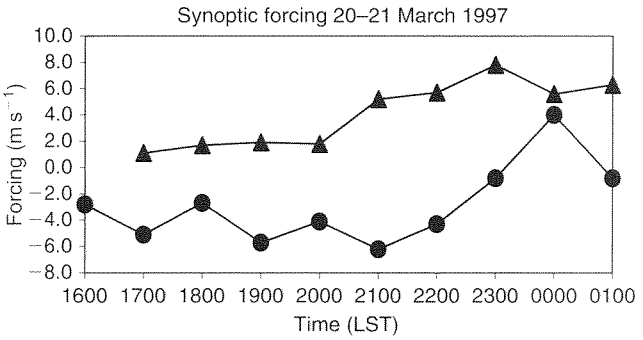

Fig. 6. Synoptic forcing for the 20 March 1997 experimental burn (circles) and for the 21 March 1997 experimental burn (triangles).

end of the valley. Smoke diversion through the side valley continued throughout the remainder of the burn (Fig. 5*b*). Model smoke also turns up the side valley and crosses the ridge through the gap at the southern end of the valley. PB-Piedmont results were nearly identical to the observed smoke movement with the exception that PB-Piedmont later allowed some smoke to drift down the valley. This reversal of the flow was partly caused when a key weather station ceased reporting hourly weather for the night. No smoke was observed down-valley from the burn site (Fig. 5*b*).

An explanation for the smoke movement observed on the evening of 20 March 1997 draws on the opposition between synoptic scale winds and drainage layer winds. As expected, drainage layer winds entrapped smoke within the stream valley. A weak low pressure center over the northern Gulf of Mexico turned the synoptic scale winds to blow from the north. These winds diminished after sunset and became light and variable during the course of the experimental burn.

However, the pressure forces that drove the synoptic scale winds did not diminish. A measure of the strength of the synoptic scale pressure forces is the 'geostrophic' wind calculated from the pressure gradients directed along the axis of a valley. The equation for synoptic forcing is

$$u_g = -\frac{R\overline{T}}{f}\frac{\Delta \ln(p)}{\Delta s}, \qquad (9)$$

where 's' is oriented parallel to the valley axis. Figure 6 shows the synoptic forcing for the night of 20 March 1997 (circles). Negative values identify when synoptic forcing favored winds blowing from the north or up-valley. Thus the synoptic forcing opposed the minuscule pressure forces that drove the drainage flows down-valley and dammed up the cooled airmasses at the south-western end of the valley. Synoptic forcing weakened after 2200 LST and became positive at midnight (when a key weather station stopped reporting) meaning that synoptic forcing favored winds blowing from the south or down-valley. Therefore, PB-Piedmont simulated smoke moving down-valley after 2300 LST.

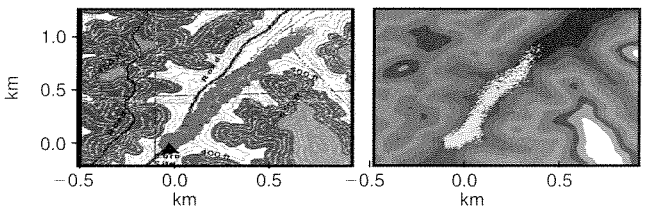

Fig. 7. Left panel: Image analysis of smoke plume at 2121 LST 21 March 1997 overlain on 30 m DEM elevation data. Right panel: PB-Piedmont simulation of smoke for the same time.

The deepened, smoke-filled drainage layer was easy to observe from the air. (An observer reported zero visibility in smoke and fog along the road leading up-valley from the burn.) However, once the smoke passed through the gap in the ridge at the southern end of the valley (Fig. 5) it was no longer visible from the air, presumably because the smoke layer became too shallow as the air accelerated downslope into the neighboring valley. A large tract of land located just south of the gap had been clear cut the previous year. Therefore, there were few if any large trees to obstruct smoke observation from the air.

21 March 1997

The procedures for conducting the experimental burn during the night of 21 March 1997 were nearly identical to those for 20 March 1997. The fire was started at the same location. Beginning at 2045 LST, Forest Service ground personnel ignited 50 bales of hay soaked in diesel fuel and detonated 60 smoke bombs. Aircraft overflights at approximately 1500 m altitude commenced at 2153 LST and continued at 7-min intervals for approximately 2 h.

The project forecast called for winds to decrease to near-calm with rapid cooling in the basin to entrap smoke there. Drainage and valley flows favored slow movement of smoke down-valley to the north-east. Figure 6 shows down-valley synoptic forcing for 21 March 1997 (triangles). Positive values mean that forcing was directed down-valley. Synoptic scale pressure forces reinforced drainage flows throughout the period of the experiment. Synoptic forcing was relatively weak (less than 2.0 m s^{-1}) until 2100 LST when forcing increased in response to an approaching weather system and remained above 5.0 m s^{-1} for the remainder of the experiment.

Figure 7 (left panel) shows the location of the smoke plume relative to the burn site and surrounding landforms at 2121 LST. The plume was defined as the locus of points taken from video imagery by image analysis methods described by Achtemeier (1998) and Achtemeier *et al.* (1998). Plume structure and orientation remained unchanged during the period of overflights. The smoke plume simulated by PB-Piedmont at 2121 LST is shown in the right panel of Fig. 7. Drainage winds confined the plume within the stream basin. The faint smoke plume was observable for a distance of ~1 km. Smoke

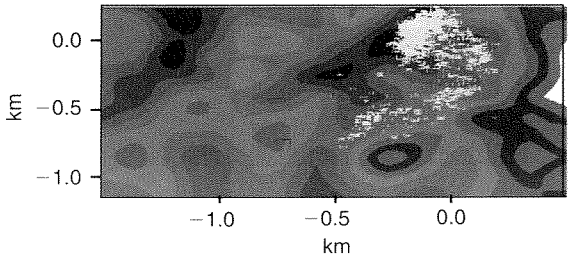

Fig. 8. Modeled smoke for 2255 LST 20 March 1997. Grid spacing is 150 m.

may have been partially obscured by overarching trees or the smoke layer thinned by spreading of the plume to the extent that smoke was no longer observable from the aircraft.

Internal validation

Critical to accurate simulations of smoke movement on the ground at night are the accuracies of underlying terrain, gradients of the atmospheric pressure at the surface used for calculating the synoptic scale forcing, and empirical cooling functions used for calculating drainage forcing. Model runs with bulk drag coefficient $C_D = 10^{-3}$ (grassland) in comparison with model runs using $C_D = 10^{-2}$ (southern pine forest) did not significantly alter either the location of the smoke plume or ridge–valley temperature lapse rates, which were critical for calculating drainage forcing.

Terrain forms the lower boundary of PB-Piedmont. If the terrain has been smoothed so that it no longer represents the terrain scales that channel smoke, then degraded performance of PB-Piedmont should be expected. Figure 8 shows model simulation of smoke for 2255 LST 20 March 1997 using a 150-m elevation grid. Figure 8 should be compared with the right panel of Fig. 5*a*. The 150-m analysis degraded the ridge located west of the valley containing entrapped smoke, effectively creating a shallower valley with slopes not as steep as those in the 30-m analysis. Smoke still was transported up-valley but the smoke was pushed to the east side of the valley and was late reaching the gap in the ridge. Additional runs with grid spacing in multiples of 30 m from 30 m to 150 m show that, for terrain characteristic of that of the Piedmont of the South, best performance is found for terrain at 30 m. Model performance degrades slowly through 150 m. For grid spacing greater than 150 m, terrain features that are important factors in the channeling of smoke may not be represented in the simulations.

Where smoke goes is determined by the sum of synoptic and drainage forcing. Synoptic scale forcing is calculated from horizontal gradients of atmospheric pressure at the surface. Horizontal pressure gradients are interpolated to the location of the burn from surface pressure data collected at surrounding weather stations. Several of these stations stopped reporting during the course of the night. Interpolated pressure data may therefore be degraded below the

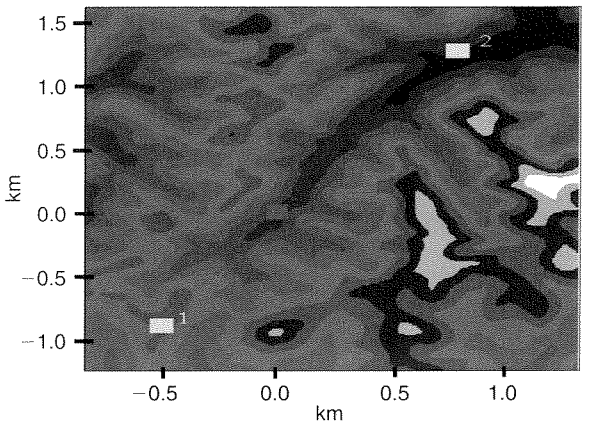

Fig. 9. Sites of two thermocouples for collecting temperature data on 20–21 March 1997 for validating PB-Piedmont. The red square identifies the burn site.

precision required for modeling smoke movement under light wind conditions. Down-valley synoptic forcing (Fig. 6) on 20 March 1997 (circles) averaged approximately $-5.0\ \mathrm{m\ s^{-1}}$ for the period 1900–2200 LST. Forcing went to zero at 2300 LST and to $+4.0\ \mathrm{m\ s^{-1}}$ at midnight after a key weather station suspended observations. These changes first left drainage forcing unopposed then reinforced down-valley forcing. PB-Piedmont moved smoke down-valley after 2300 LST (see top of right panel Fig. 5*b*). Neither did members of the burn crew nor personnel on board the aircraft observe smoke moving down-valley from the burn site. The inference from the continued transport of smoke up-valley after 2200 LST is that the synoptic scale forcing continued at approximately the same sign and magnitude for the next several hours.

As regards drainage forcing, cooling functions set forth in equation (3) determine the maximum rate of cooling and maximum lapse rate of temperature allowed for the drainage layer, $2.78 \times 10^{-3}\ \mathrm{K\ s^{-1}}$ and $0.1667\ \mathrm{K\ m^{-1}}$ respectively. However, the maximum lapse rate is not always attained. If the model lapse rate is, for example, less than the ambient lapse rate, then the model surface temperature is too warm relative to the temperature of the air just above the drainage layer. This means that the drainage flow is too weak and more likely to be dominated by synoptic forcing. Thus comparisons between the model-generated lapse rates and observed lapse rates provide an independent validation for PB-Piedmont regarding the strength of drainage flows.

Two temperature sensors were placed at different elevations along a road that ran from a ridge at the south end of the valley through the burn site (Fig. 9). The measurements were taken with thermocouples positioned ~1 m above ground. One sensor was located at the top of the ridge (146 m) south of the burn site and the other in the valley (91 m). The lapse rate of temperature was calculated as the difference between the observed temperature at the ridge top and the observed temperature in the valley divided by the difference in sensor

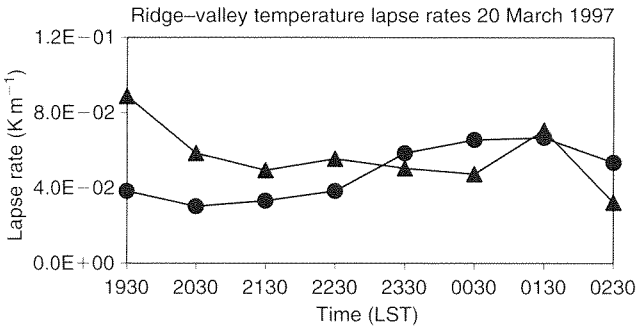

Fig. 10. Ridge–valley lapse rates of temperature (K m^{-1}) modeled (triangles) and observed (circles) for 20 March 1997. Lapse rates calculated from temperatures and elevations at sites 1 and 2 (see Fig. 9).

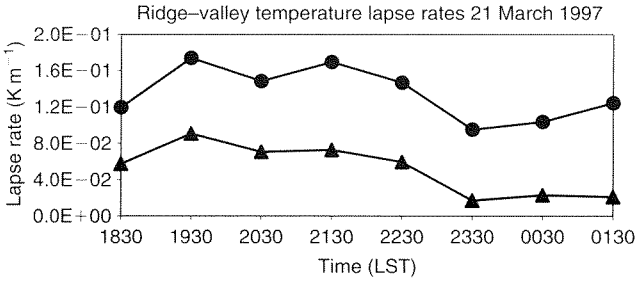

Fig. 11. Ridge–valley lapse rates of temperature (K m^{-1}) modeled (triangles) and observed (circles) for 21 March 1997. Lapse rates calculated from temperatures and elevations at sites 1 and 2 (see Fig. 9).

elevation. The PB-Piedmont lapse rate of temperature was taken as the difference between model-simulated surface temperatures at the ridge top and at the same location in the valley divided by the difference in elevation.

Figure 10 compares modeled with observed lapse rates of temperatures for 20 March 1997 for the period including the project overflights. All modeled and observed lapse rates were inversions. The model lapse rate of temperature at 1930 LST was approximately half of the maximum allowable yet was twice as great as the observed lapse rate of temperature. This means that the model was over-predicting the strength of the drainage forcing. The model lapse rate converged toward the observed lapse rate so that from 2130 LST on, correspondence was fairly good. Corrections for saturation were in effect from 2130 LST. Valley fogs were observed during the night of March 20.

Modeled and observed lapse rates of temperature were in excellent agreement for the first 3 h after sunset on 21 March (Fig. 11). Thereafter, model lapse rates of temperature decreased relative to the observed lapse rates of temperature. From Fig. 6, down-valley synoptic forcing increased beginning at 2100 LST. The impact of the larger synoptic forcing was to push the drainage air down-valley. Analysis of the drainage layer depth from 2100 LST to 2330 LST showed that the depth decreased by ~10 m. The drainage layer was being pushed down-valley faster than the drainage layer was being replenished. Thus the model was under-predicting the depth of the drainage layer.

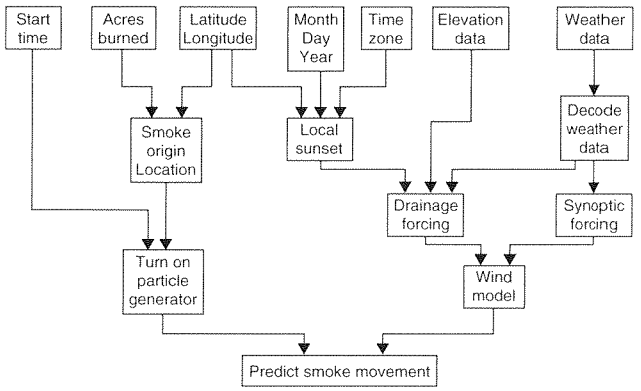

Fig. 12. Flow diagram showing inputs and key steps in PB-Piedmont for short-range predictions of smoke movement.

Comparisons with model-predicted smoke and observations of smoke in Figs 4, 5 and 7 suggest that the differences between the modeled and observed lapse rates of temperature in the drainage layers did not decrease the accuracy of the model predictions.

Discussion

PB-Piedmont is a time-dependent wind and smoke simulation model designed to aid the land manager in tracking the movement of residual smoke at night given that residual smoke is in fact present. Land managers experienced with tracking smoke on the ground at night know that wind reports from distant weather stations are often not representative of on-site air movement. PB-Piedmont provides critical numerical 'eyes' to 'see' where smoke is moving at night. Thus the model gives guidance on where smoke might be going.

Smoke observations and results from model simulations show that smoke movement at night over the Piedmont is a complex interaction between terrain and meteorology that cannot be easily anticipated by land managers. Ridge–valley elevation differences, small gaps in ridges and valley orientation with respect to other valleys and prevailing winds are factors in smoke transport. Synoptic forcing must reinforce drainage flows in some valleys and oppose drainage forcing in other valleys. Both synoptic forcing and drainage forcing are time dependent. Synoptic forcing changes as weather systems pass by during typical 10–12 h night-time periods. Drainage forcing depends on the depth of the drainage layer, cooling rates and moisture.

PB-Piedmont does not predict smoke concentrations. Emissions from residual smoke over a burn area are usually unknown. However, an advantage to this deficiency is that the inputs to the model are simple. User-defined inputs (Fig. 12) are limited to burn start time, acres burned, latitude and longitude of the burn site, the month, day, and year, and the time zone. The inputs are used to calculate local sunset,

locate the smoke origin grid, and turn on the particle generator. Elevation data are provided with the model. Weather data are available from select Internet sites.

This paper has presented the modeling philosophy for PB-Piedmont, the mathematical development of the model, and tests of the model using for validation aircraft video imaging of plumes from two experimental burns at night. These tests showed that the model performs well for drainage flows late in the evening.

Acknowledgements

I acknowledge Ken Forbus, Tim Giddens, Pat Outcalt and Wayne Adkins (ret.) of the Southern Research Station Smoke Management Team for technical and electronic contributions that made possible the smoke projects that defined and validated PB-Piedmont. The USDA Forest Service Remote Sensing Applications Center is acknowledged for loan of a light-sensitive, multi-spectral camera used for aircraft overflights. The USDA Forest Service Region 8 Fire & Aviation is acknowledged for providing an aircraft for experimental burn overflights. Also, ground crews at the Talladega National Forest in Alabama, Oakmulgee Ranger District are acknowledged for initiating and maintaining smoke sources. Funding was provided through the National Fire Plan 01.SRS.A.5.

References

Achtemeier GL (1979) Evaluation of operational streamline methods. *Monthly Weather Review* **107**, 198–206. doi:10.1175/1520-0493(1979)107<0198:EOOOSM>2.0.CO;2

Achtemeier GL (1987) On the concept of varying influence radii for a successive corrections objective analysis. *Monthly Weather Review* **115**, 1760–1771. doi:10.1175/1520-0493(1987)115<1760:OTCOVI>2.0.CO;2

Achtemeier GL (1989) Modification of a successive corrections objective analysis for improved higher order calculations. *Monthly Weather Review* **117**, 78–86. doi:10.1175/1520-0493(1989)117<0078:MOASCO>2.0.CO;2

Achtemeier GL (1991) Reducing hydrostatic truncation error in a meso-beta boundary layer model. *Monthly Weather Review* **119**, 223–229. doi:10.1175/1520-0493(1991)119<0223:RHTEIA>2.0.CO;2

Achtemeier GL (1993) Measurements of drainage winds along a small ridge. In 'Proceedings of the 86th Annual Meeting and Exhibition'. Air & Waste Management Association, 93-FA-155.06O. 15 pp.

Achtemeier GL (1994) Contrasts in objective analysis philosophy: Comments on 'The theoretical, discrete, and actual response of the Barnes objective analysis scheme for one- and two-dimensional fields'. *Monthly Weather Review* **122**, 397–398. doi:10.1175/1520-0493(1994)122<0397:CIOAPC>2.0.CO;2

Achtemeier GL (1998) First remote measurements of smoke on the ground at night. Second Symposium on Fire and Forest Meteorology, 11–16 January 1998, Phoenix, AZ. American Meteorological Society, pp. 165–169.

Achtemeier GL, Adkins CW, Greenfield PH (1998) Airborne mapping of near-ground smoke at night using GPS and light-enhancing video imagery. Proceedings of the Seventh Forest Service Remote Sensing Applications Conference, 6–10 April 1998, pp. 317–327. (American Society for Photogrammetry and Remote Sensing: Bethesda, MD)

Barnes SL (1964) A technique for maximizing details in numerical weather map analysis. *Journal of Applied Meteorology* **3**, 396–409. doi:10.1175/1520-0450(1964)003<0396:ATFMDI>2.0.CO;2

Barnes SL (1973) 'Mesoscale objective analysis using weighted time-series observations.' NOAA Technical Memorandum ERL NSSL-62. NTIS COM-73–10781. 60 pp. (National Severe Storms Laboratory: Norman, OK)

Barnes SL (1994) Applications of the Barnes objective analysis scheme. Part III: Tuning for minimum error. *Journal of Atmospheric and Oceanic Technology* **11**, 1459–1479. doi:10.1175/1520-0426(1994)011<1459:AOTBOA>2.0.CO;2

Caracena F (1987) Analytic approximation of discrete field samples with weighted sums and the gridless computation of field derivatives. *Journal of Atmospheric Sciences* **44**, 3753–3768. doi:10.1175/1520-0469(1987)044<3753:AAODFS>2.0.CO;2

Clements WE, Archuleta JA, Hoard DE (1989) Mean structure of the nocturnal drainage flow in a deep valley. *Journal of Applied Meteorology* **28**, 457–462. doi:10.1175/1520-0450(1989)028<0457:MSOTND>2.0.CO;2

Garrett AJ, Smith FG, III (1984) Two-dimensional simulations of drainage winds and diffusion compared to observations. *Journal of Climate and Applied Meteorology* **23**, 597–610. doi:10.1175/1520-0450(1984)023<0597:TDSODW>2.0.CO;2

Gudiksen PH, Leone JM, Jr, King CW, Ruffieux D, Neff WD (1992) Measurements and modeling of the effects of ambient meteorology on nocturnal drainage flows. *Journal of Applied Meteorology* **31**, 1023–1032. doi:10.1175/1520-0450(1992)031<1023:MAMOTE>2.0.CO;2

King CW (1989) Representativeness of single vertical wind profiles for determining volume flux in valleys. *Journal of Applied Meteorology* **28**, 463–466. doi:10.1175/1520-0450(1989)028<0463:ROSVWP>2.0.CO;2

Lavdas L, Achtemeier GL (1995) A fog and smoke risk index for estimating roadway visibility hazard. *National Weather Digest* **20**, 26–33.

McKee TB, O'Neal RD (1989) The role of valley geometry and energy budget in the formation of nocturnal valley winds. *Journal of Applied Meteorology* **28**, 445–456. doi:10.1175/1520-0450(1989)028<0445:TROVGA>2.0.CO;2

Mobley HE (1989) 'Summary of smoke-related accidents in the South from prescribed fire (1979–1988).' American Pulpwood Association Technical Release 90-R-11.

Neff WD, King CW (1989) The accumulation and pooling of drainage flows in a large basin. *Journal of Applied Meteorology* **28**, 518–529. doi:10.1175/1520-0450(1989)028<0518:TAAPOD>2.0.CO;2

O'Steen LB (2000) Numerical simulation of nocturnal drainage flows in idealized valley-tributary systems. *Journal of Applied Meteorology* **39**, 1845–1860. doi:10.1175/1520-0450(2000)039<1845:NSONDF>2.0.CO;2

Papadopoulos KH, Helmis CG (1999) Evening and morning transition of katabatic flows. *Boundary-Layer Meteorology* **92**, 195–227. doi:10.1023/A:1002070526425

Pauley PM, Wu X (1990) The theoretical, discrete, and actual response of the Barnes objective analysis scheme for one- and two-dimensional fields. *Monthly Weather Review* **118**, 1145–1163. doi:10.1175/1520-0493(1990)118<1145:TTDAAR>2.0.CO;2

Post MJ, Neff WD (1986) Doppler lidar measurements of winds in a narrow mountain valley. *Bulletin of the American Meteorological Society* **67**, 274–281. doi:10.1175/1520-0477(1986)067<0274:DLMOWI>2.0.CO;2

Ritchie H (1986) Eliminating the interpolation associated with the semi-Lagrangian scheme. *Monthly Weather Review* **114**, 135–146. doi:10.1175/1520-0493(1986)114<0135:ETIAWT>2.0.CO;2

Sakiyama SK (1990) Drainage flow characteristics and inversion breakup in two Alberta mountain valleys. *Journal of Applied Meteorology* **29**, 1015–1030. doi:10.1175/1520-0450(1990)029<1015:DFCAIB>2.0.CO;2

Scott RW, Achtemeier GL (1987) Estimating pathways of migrating insects carried in atmospheric winds. *Environmental Entomology* **16**, 1244–1254.

Staniforth A, Cote J (1991) Semi-Lagrangian integration schemes for atmospheric models—a review. *Monthly Weather Review* **119**, 2206–2223.

Thompson PD (1952) 'Notes on the theory of large-scale disturbances in atmospheric flow with applications to numerical weather prediction.' Geophysical Research Papers No. 16. (Geophysics Research Directorate: Cambridge, MA)

Winstead NS, Young GS (2000) An analysis of exit-flow drainage jets over the Chesapeake Bay. *Journal of Applied Meteorology* **39**, 1269–1281. doi:10.1175/1520-0450(2000)039<1269:AAOEFD>2.0.CO;2

Varvayanni M, Bartzis JG, Catsaros N, Deligiannis P, Elderkin CE (1997) Simulation of nocturnal drainage flows enhanced by deep canyons: the Rocky Flats case. *Journal of Applied Meteorology* **36**, 775–791.

Appendix 1

The Gaussian function weights each datum inversely proportional to the square of its distance (r) from a grid point by

$$wt = \exp\left[\frac{-r^2}{4k}\right], \tag{A1}$$

where k is a shape factor for the weighting curve and therefore determines how smoothing will cause the final analysis to depart from the original data field. If $f(x, y)$ describes a field of data, then application of equation (A1) will generate a new function $g(x, y)$ such that,

$$g(x, y) = D_0(a, k)f(x, y), \tag{A2}$$

where $D_0(a, k)$ is a response function. Barnes (1964) showed that

$$D_0(a, k) = \exp(-a^2k), \tag{A3}$$

if the original data field is described by the function

$$f(x, y) = A\sin(ax),$$

where

$$a = 2\pi/\lambda \tag{A4}$$

and λ refers to wavelength. The optimal response for the 2-pass successive corrections Gaussian objective analysis is

$$B = D_0(2 - D_0) = 2D_0 - D_0^2 \tag{A5}$$

(Achtemeier 1987). To create the A-Function, add a constant to the original function so that

$$F(x, y) = C_0 + f(x, y). \tag{A6}$$

Then, using equation (A1), perform two separate single-pass interpolations with different k to yield two new functions:

$$\begin{aligned} G_1(x, y) &= D_1(a, k_1)F(x, y) \\ G_2(x, y) &= D_2(a, k_2)F(x, y). \end{aligned} \tag{A7}$$

The A-Function is defined as the ratio of the square of G_2 to G_1 and subtracting the constant:

$$F = \frac{G_2^2}{G_1} - C_0. \tag{A8}$$

The response equation for the A-Function is

$$R = \frac{(C_0 + D_2f(x, y))^2}{C_0 + D_1f(x, y)} - C_0, \tag{A9}$$

where the response function for $C_0 = 1$. Expanding equation (A9) yields

$$R = \frac{C_0(2D_2f(x, y) - D_1f(x, y)) + (D_2f(x, y))^2}{C_0 + D_1f(x, y)}. \tag{A10}$$

The response equation for the A-Function is a complex summation of products of functions with response functions. In addition, the presence of the second term in the denominator of equation (A10) acts to increase (decrease) the estimate for R depending on whether the sign of the term is negative (positive). This problem can be solved and equation (A10) simplified by choosing for C_0 a value that is much greater than the amplitude of $f(x, y)$. Thus terms not multiplied by C_0 can be neglected in equation (A10). Furthermore, from equation (A7) and the definition in equation (A3), let $k_1 = 2k_2$. Then

$$R = (2D_2 - D_2^2), \tag{A11}$$

which is equivalent to equation (A5). Thus the A-Function has the same response as the optimal 2-pass Gaussian method but without the additional interpolation.